ELSEVIER

Journal of Cereal Science 43 (2006) 70–78

Journal of CEREAL SCIENCE

www.elsevier.com/locate/jnlabr/yjcrs

NMR imaging of developing barley grains

S.M. Glidewell*

Scottish Crop Research Institute, Invergowrie, Dundee DD2 5DA, UK

Received 23 March 2005; revised 27 June 2005; accepted 25 July 2005

Abstract

NMR imaging was used for the non-invasive acquisition of three-dimensional images of developing barley grains from anthesis to maturity, 40 days after anthesis. Quantitative T_2 maps were generated, and chemical shift imaging detected changes in the tissue distribution of water, soluble carbohydrate and lipids. Complete 3D data are accessible on a website.

Keywords: Anatomy; Caryopsis; Magnetic resonance imaging; Non-invasive

1. Introduction

World production of barley in 2003 ((FAOSTAT, 2004) was 142 million metric tonnes, around a quarter of that of maize, rice or wheat; in the UK, barley represents around 30% of the cereal crop of which 80% goes as animal feed and 20% for malting. Of the malting barley used in the UK, around 55% goes for brewing and 37% for distilling (The Maltsters Association of Great Britain, 2004).

The malting process is of great commercial significance and good malting barley requires an even modification of endosperm which depends, at least in part, on the water distribution. Non-invasive investigations of the initial step of water uptake (McEntyre et al., 1998; Molina-Cano et al., 2002), and malting quality (Gruwel et al., 2002) have been made using NMR imaging (also known as MRI). Water uptake in maize, where steeping is a pre-requisite for wet-milling, has also been studied by NMR imaging (Ruan et al., 1992; Ruan and Litchfield, 1992). Wheat dormancy and rice cooking (Himmelsbach and Gamble, 1996; Horigane et al., 1999, 2000; Takeuchi et al., 1997), maize maturity (including T_2 as a parameter (Ruan et al., 1999) have also been studied by NMR imaging. The technique has been used to image the location of sugars in germinating barley (Ishida et al., 1996) and the anatomical development of rice caryopses (Horigane et al., 2001).

Proton NMR imaging detects mobile molecules containing hydrogen. In most fresh plant material, water contributes most of the signal. The relative intensity of different regions of an image depends not only on the total concentration of mobile protons, but also on the rate at which they relax after stimulation, as a function of the experimental parameters used. The 3D images were acquired with as little relaxation weighting as possible and thus approximate the distribution of mobile protons. The relaxation parameter T_2, or spin-spin relaxation time, is a function of the rate at which the nuclear spins exchange energy between themselves, and is affected by molecular mobility, as well as by the presence of paramagnetic ions or magnetic susceptibility discontinuities. For further details of NMR imaging see Glidewell et al. (1997); Chudek and Hunter (1997) or, for a more technical approach, Callaghan (1993).

In the present study the detailed 3D anatomy of the barley caryopses from anthesis to maturity was followed using single spikelets rather than entire spikes as used by Kano et al. (1990). By creating quantitative T_2 maps and chemical shift images the distribution of water, soluble carbohydrates and lipids were detected separately. The NMR spectra revealed the relative concentrations of the three classes of compounds in the different tissues of the grain.

Abbreviations: CPMG, Carr-Purcell-Meiboom-Gill; daa, days after anthesis; Gd-DTPA, gadolinium(III)-diethylene-triamine pentaacetic acid; MIP, maximum intensity projection; MRI, magnetic resonance imaging; NMR, nuclear magnetic resonance; ppm, parts per million; RF, radio-frequency; T, Tesla; TMS, tetramethylsilane.

* Corresponding author. Tel.: +44 1382 562731; fax: +44 1382 568516.
E-mail address: sglide@scri.ac.uk.

0733-5210/$ - see front matter © 2005 Elsevier Ltd. All rights reserved.
doi:10.1016/j.jcs.2005.07.003

2. Experimental

2.1. Plant material

Barley (*Hordeum vulgare* L.) cv Optic plants were grown in pots in a glasshouse and scored daily for anthesis. Spikes at the appropriate development stage were selected and removed to the laboratory. A representative spikelet was selected from the central region of the spike for NMR imaging.

2.2. NMR imaging

Individual spikelets up to 12 daa were placed in a 5 mm NMR tube and held vertically by a capillary containing 1 mM Gd-DTPA which was used as an intensity scale object. A small piece of wet tissue was held inside the plastic cap of the tube to maintain a moist atmosphere in the tube which was imaged in a 5 mm diameter saddle RF coil. For spikelets >12 daa, an 8 mm i.d. tube was used in a 10 mm diameter RF coil. NMR images were acquired at 7.1 T in a Bruker AMX300 SWB instrument (Bruker BioSpin, Coventry, UK) using a microimaging probe. 3D spin echo datasets were acquired with an echo time (TE) of 6.56 ms and a repeat time (TR) of 500 ms. For selected spikelets, T_2 images of selectively excited 2 mm slices were acquired using a Carr-Purcell-Meiboom-Gill (CPMG) (Meiboom and Gill, 1958) pulse sequence of 12 echoes at 8.28 ms intervals and a TR of 5000 ms. Chemical shift images were also acquired of selectively excited 500 μm slices of spikelets. Voxel sizes were $(47–62.5\ \mu m)^3$ for the 3D images; pixel sizes were $(47–62.5\ \mu m)^2$ for the transverse T_2 images and approximately twice that for the chemical shift images which were zero-filled from 64×64 matrices. Data were processed initially using UXNMR (Bruker) on the AMX300 or ParaVision (Bruker) on a Silicon Graphics O2. The original 32-bit images were intensity-scaled using the Gd-DTPA phantom to 8-bit images. Chemical shift and T_2 images were produced with WinMRI (Bruker) running on a PC. SlicerDicer (Pixotec, Renton, WA. USA) and Animation Shop (Jasc, Eden Prairie, USA) were used to generate the animations.

3. Results and discussion

The complete 3D images are available for viewing at http://www.scri.sari.ac.uk/bardev/index.htm and show viewer-controllable step-through images in three mutually orthogonal directions and rotating maximum intensity projections. Selected frames from the 3D images are shown in Fig. 1 for time points from 0–40 daa. Fig. 2 shows T_2 maps and total proton images for selected time points and Figs. 4 and 5 show chemical shift images and spectra, respectively.

3.1. Anatomical images

Identification of the anatomical features was made, principally, with reference to Briggs (1978); Allen et al. (2000); Wallwork et al. (1998).

The two stills (Fig. 1a,b) from the maximum intensity projection (MIP) animation show the anthers being ejected and their path can be followed in Fig. 1.1a–d. In transverse section (Fig. 1e,h), the palea and lemma are clearly seen including the vascular bundles in the lemma. The feathery stigmas remain visible in the MIPs until 8 daa (Fig. 1.8b) (Briggs and Briggs, 1978). The funiculus is visible in the MIPs up to 6 daa and also in the sequential longitudinal slices until 10 daa. The sequential transverse slices at 2, 4 and 6 daa show the vascular traces in the pericarp. Slices near the median show darker regions around the vascular traces at 6 daa, possibly corresponding to increased starch deposition (Weschke et al., 2000) compared to 2 and 4 daa.

At 4 daa (Fig. 1.4g), the embryo sac is breaking out of the ovary, whose wall will form the pericarp and ultimately fuse with the palea and lemma. The higher resolution afforded by a 2D transverse slice selective image (Fig. 1.6i) shows the aleurone layer around the endosperm which is still delineated from the pericarp, and the initiation of the scutellum separating the endosperm from the embryo. Bosnes et al. (1992) report aleurone cell differentiation at 8 days after pollination. By 8daa, the scutellum is visible in the MIP (Fig. 1.8b) and the embryo sac has elongated to fill the length of the space enclosed by the palea although there is still a gap around the circumference of the embryo sac which will not be fully adpressed to the palea until 12 daa (Fig. 1.12d,e).

By 12 daa, the general shape of the caryopsis is finalised and the endosperm enlarges circumferentially as the embryo grows and its shape becomes more readily discerned. At 16 daa (Fig. 1.16c,d) the plumule and radicle are clearly seen and individual rootlets are seen from this time (Fig. 1.16d,e). The amount of water in the endosperm and the crease declines during development until at maturity (40daa) the embryo is the brightest region of the image (Fig. 1.40d).

In contrast to the findings of Horigane et al. (2001) in rice, the vascular bundles in the palea are still visible in transverse slices at 40 daa and the vascular bundle of the pericarp remained very bright until maturity at 40 daa; this is probably due largely to the presence of the ventral crease in barley, a feature which is absent in rice. As in rice, bright areas around the crease indicate the movement of water and presumably nutrients into the endosperm (Cochrane and Duffus, 1980; Cook and Oparka, 1983).

Song et al. (1998) ascribe a dark area in longitudinal slices of a mature wheat grain to the crease and attribute

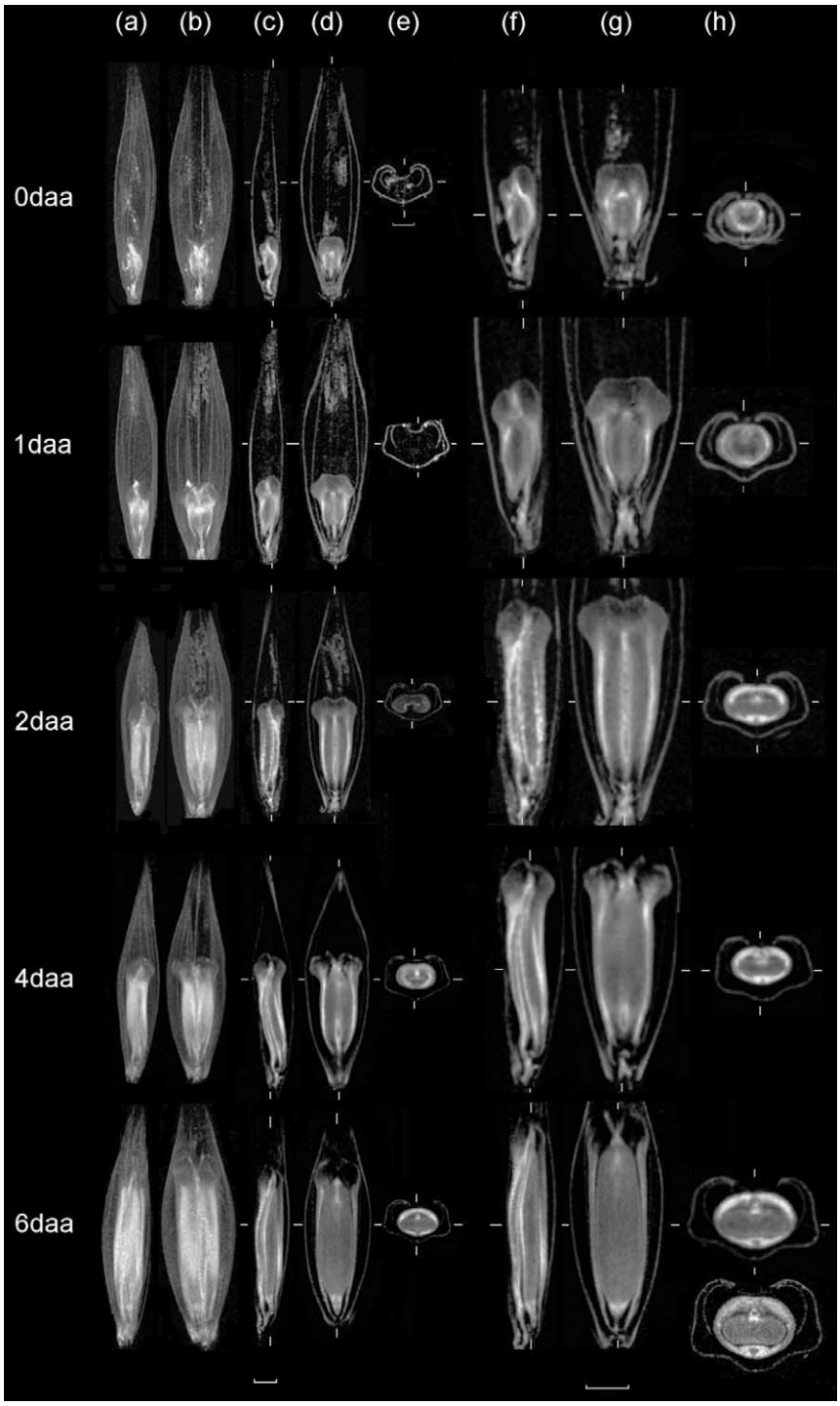

Fig. 1.0. 0 daa (a) dorso-ventral, (b) lateral maximum intensity projections; (c) dorso-ventral, (d) lateral, (e) transverse median slice; (f), (g), (h) enlargements of (c), (d), (e), respectively. The white bars on the median slices indicate the position of the other two orthogonal slices. (1.1) 1 daa (a)–(h) as Fig. 1.0. (1.2) 2 daa (a)–(h) as Fig. 1.0. (1.4) 4 daa (a)–(h) as Fig. 1.0. (1.6) 6 daa (a)–(h) as Fig. 1.0. Scale bars 1 mm.

the bright adjacent area assigned as the crease in Fig. 1*c, to surface water condensate. It is obvious from observations of the crease tissue at different developmental stages that, at least in barley as observed here, the bright area is an intrinsic part of the grain.

3.2. T_2 maps

In general, the T_2 values mirror the total proton content but there are a few instances where they diverge, e.g. at 21 daa, when the crease has a higher proton content than

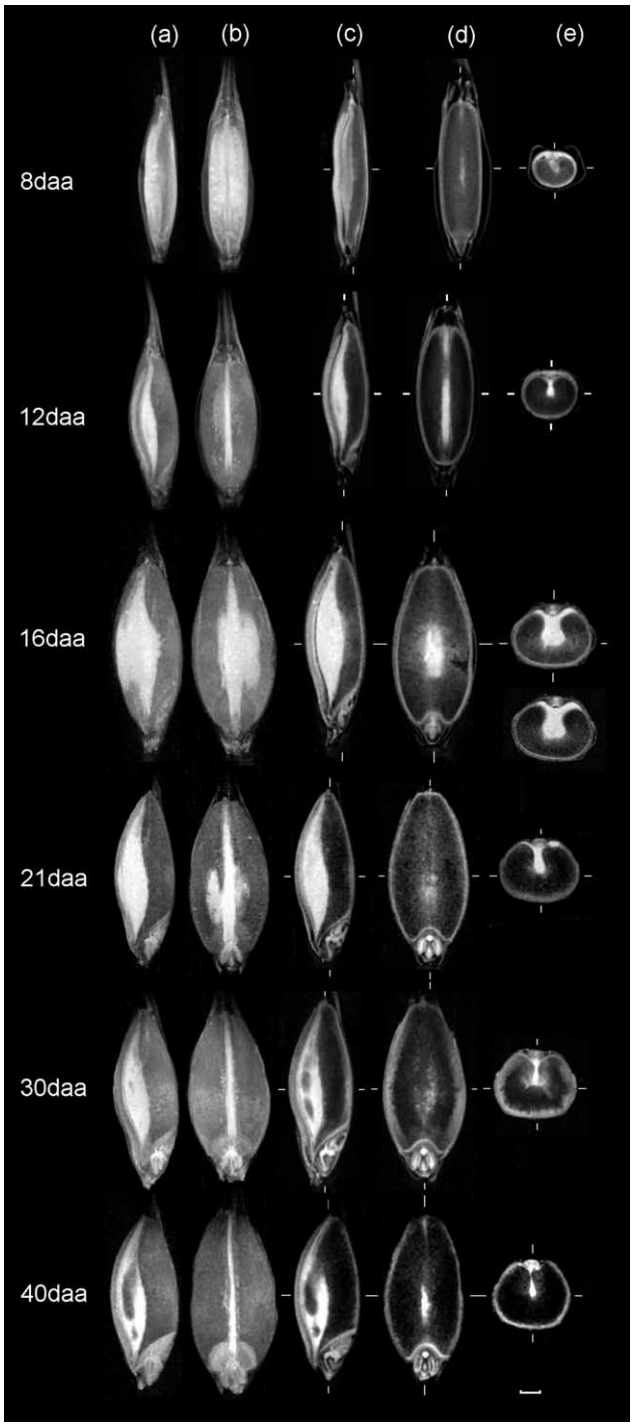

Fig. 1.8. 8 daa (a)–(e) as Fig. 1.0. (1.12) 12 daa (a)–(e) as Fig. 1.0. (1.16) 16 daa (a)–(e) as Fig. 1.0. (1.21) 21 daa (a)–(e) as Fig. 1.0. (1.30) 30 daa (a)–(e) as Fig. 1.0. (1.40) 40 daa (a)–(e) as Fig. 1.0. All scale bars 1 mm.

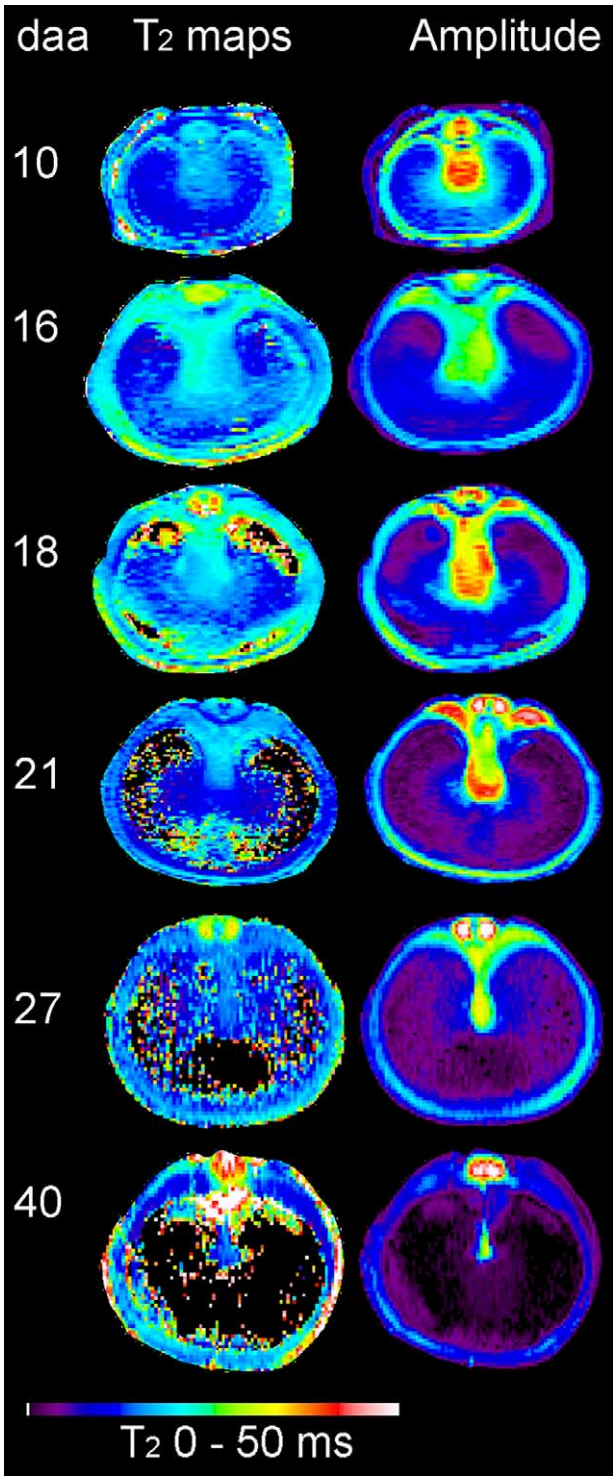

Fig. 2. T_2 and amplitude maps of median transverse slices of barley grains at a range of days after anthesis. Black or speckled areas on the T_2 maps are areas where the program was unable to fit the data to the exponential decay formula. These areas correspond to areas of low total imageable proton concentration.

the tissue between the crease and the nucellar projection, whereas the reverse is true of the same areas of the T_2 map. Up to 18 daa, the crease region has a total proton content similar to that of the nucellar projection and vascular bundle, whereas the T_2 of the crease tissue is always less than that of these regions. At the later developmental stages, the crease region shows a lower relative intensity on both parameter images.

Low values of T_2, in the range of ~5–45 ms, were observed, despite the use of a CPMG (Meiboom and Gill,

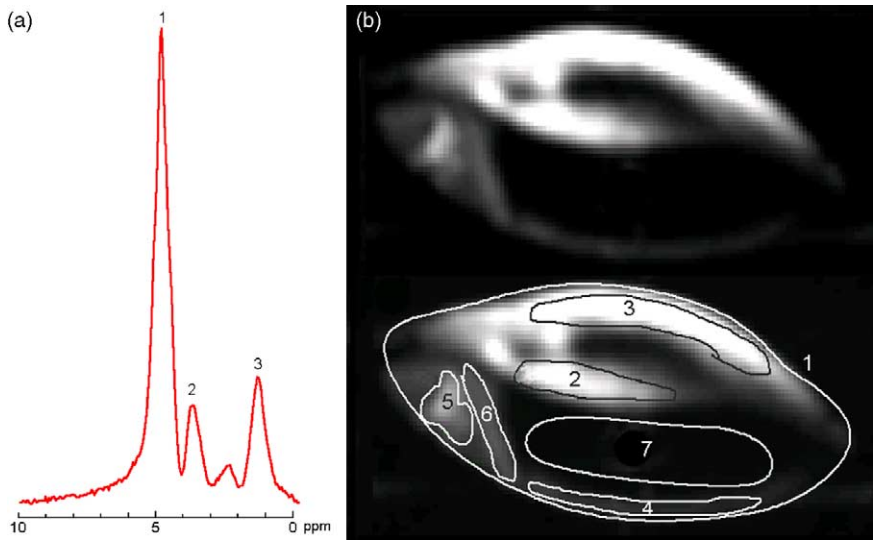

Fig. 3. (a) NMR spectrum of embryonic node of 40 daa caryopsis showing spectral regions in Fig. 4: (1) water (w); (2) sugars (s); (3) lipids (l). (b) Median longitudinal slice of 40 daa caryopsis at all spectral frequencies showing regions as defined for spectra in Fig. 5: (1) whole slice (wh); (2) crease (cr); (3) ventral wall (vw); (4) dorsal wall (dw); (5) embryo (em); (6) scutellum (sc), (7) endosperm (en).

1958) pulse sequence to remove the dephasing effect of local magnetic susceptibility discontinuities (Glidewell et al., 1999) which arise from the presence of intercellular gas spaces typical of plant tissue. As the caryopsis matures, the endosperm in particular, dries out and, although the remaining starch has a high concentration of protons, their mobility and that of the remaining water protons is restricted by hydrogen bonding so that their T_2 becomes too low for the detection of an NMR signal using the parameters allowable by the hardware and software of the instrument. Donker et al. (1996, 1997) point out that T_2 images are best acquired at low field using a multi-echo sequence with a short echo time. Most laboratories do not have a choice of field strength available and hardware constraints limit the minimum echo time as a function of the spatial resolution, so a compromise has to be made between discerning anatomical features and solving the parameter fit for T_2. The use of false colour accentuates the pattern of water distribution in the endosperm and shows its decrease starting in the centre of the endosperm mass and moving towards the aleurone layer and the crease as grain filling proceeds. By maturity at 40 daa, the T_2 of the endosperm is too low for the software to solve for a T_2 map although the value of T_2 in the transverse slice of the nucellar projection and vascular bundle is at its highest, indicating the patency of these tissues. A peripheral vascular strand in the lemma is visible at the base of the amplitude image at 40 daa.

3.3. Chemical shift imaging

The resonance frequency of an atomic nucleus depends on its intrinsic properties and the magnetic field at the nucleus. Protons (hydrogen nuclei) resonate at around 300 MHz in a magnetic field of 7.1 T. Variations of the order of parts per million (ppm) occur as a result of differences in the electronic environment of protons depending on their position in a molecule. Thus, protons in lipid molecules are more shielded from the external magnetic field by their electrons than protons in water molecules whose electrons are delocalised towards the oxygen atom. Protons in water thus resonate at a slightly different frequency from those in lipids. This is referred to as the chemical shift of a resonance and for protons, is measured in parts per million from tetramethylsilane (TMS) at 0 ppm. Chemical shift imaging acquires an NMR spectrum for each pixel of the image and an image for each frequency sampling range. For instance, in these experiments, the frequency range was 4000 Hz over 256 points giving an image for each 15.625 Hz. Software allows the selection of regions of interest in either the image or the spectrum to be defined and the corresponding spectrum or image to be displayed. The chemical shift images presented here have been derived from spectral regions corresponding to water, soluble carbohydrates and lipids as indicated in Fig. 3a. The spatial regions of a median longitudinal slice giving rise to NMR spectra are shown in Fig. 3b.

3.3.1. Chemical shift images

The lipid image at 10 daa (Fig. 4.10l) has a relatively high intensity in the embryo and the crease; however, the spectrum of the crease shows no lipid peak and the intensity in the lipid image arises from the shoulder of the large water peak. In contrast, although the spectrum of the embryo (Fig. 5.10em) looks similar at first, there is a small signal in the lipid region when the gain is increased. There is however, very little difference visible in the distribution of water, soluble carbohydrate and

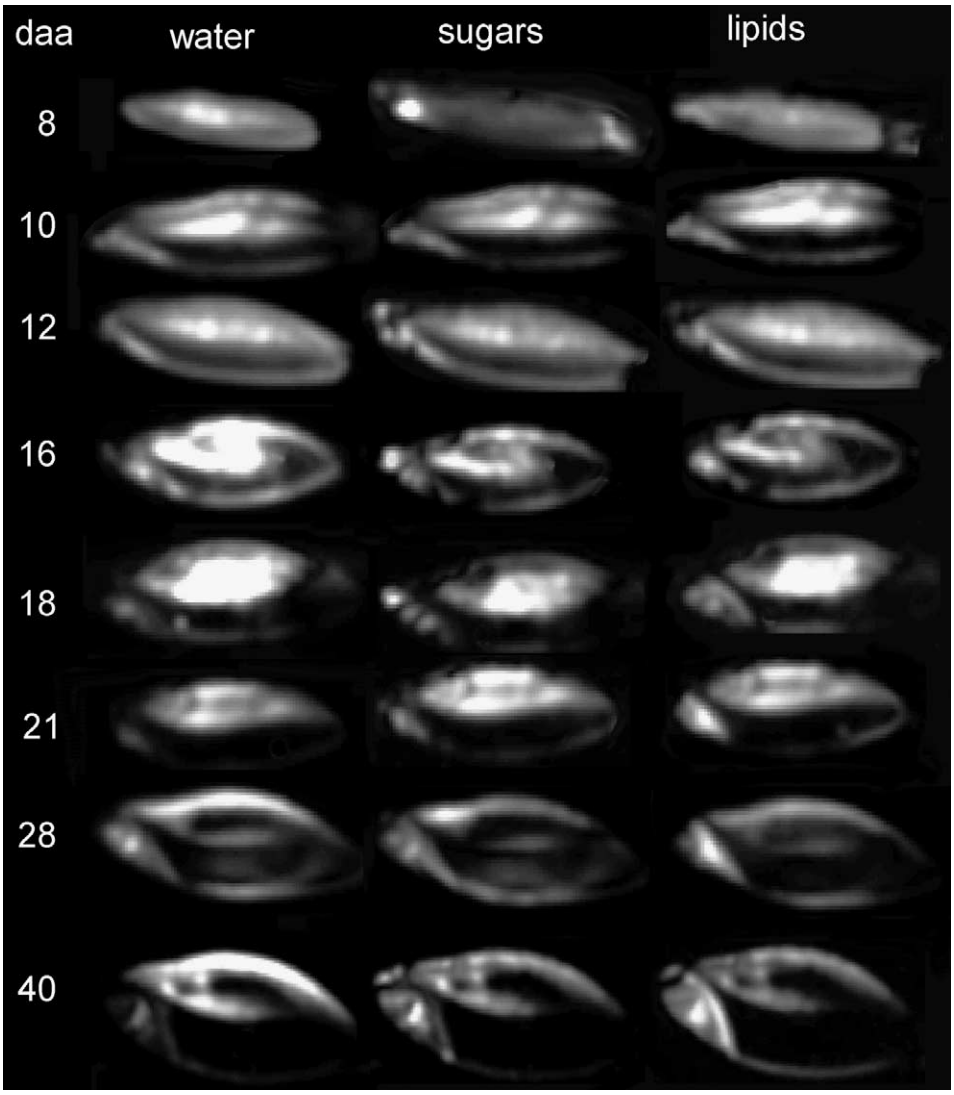

Fig. 4. Chemical shift images of a longitudinal median 500 μm slices of barley caryopses at indicated number of days after anthesis.

lipids at 10 daa as the principal signal is from water. While it is possible to suppress the water signal, at least to some extent (Xia and Jelinski, 1995), it was also of interest in this study to map the water distribution. By 12 daa, there is a slight difference in the chemical shift images (Fig. 4.12) and lipid and soluble carbohydrate are more prominent in the embryo and sugars in the funiculus. At 16 daa, there are clear differences in the images (Fig. 4.16) and although the crease and pericarp regions, as well as the embryo, appear bright in the lipid image, only the embryo shows a lipid peak in its spectrum (Fig. 5.16em).

A similar situation obtains at 18 daa when the embryo and scutellum clearly show a lipid image (Fig. 4.18l) but to a lesser extent in other tissues (Fig. 4.18w, s). The spectra of the embryo (Fig. 5.18em) and scutellum (Fig. 5.18sc) clearly indicate that there is water present, but not at such a high level as in the other tissues. The high intensity in the crease region in the lipid image (Fig. 4.18l) does not in fact come from lipid, as indicated by the absence of a lipid peak in the spectrum (Fig. 5.18cr), but from the 'tail' of the large water peak (Fig. 5.18cr).

At 21 daa, there is a clear difference in the embryo region between the chemical shift selective images, showing high soluble carbohydrate in the central region of the embryonic axis (Fig. 4.21s) and higher lipid in the scutellum (Fig. 4.21l). The spectrum (Fig. 5.21cr) of the crease shows low soluble carbohydrate and no lipid relative to the large water signal, whereas the embryonic axis (Fig. 5.21em) and scutellum (Fig. 5.21sc) show clear soluble carbohydrate and lipid peaks. At the same gain as the spectrum of the scutellum (Fig. 5.21sc), the spectrum of the crease (Fig. 5.21cr) shows the slightest trace of lipid compared with the spectra of the scutellum, embryo and dorsal wall regions (Fig. 5.21em, dw).

By 28 daa, the cotyledonary node of the embryo (after Fahn, 1967) is delineated in water and soluble carbohydrate images (Fig. 4.28w,s) and the whole embryonic region

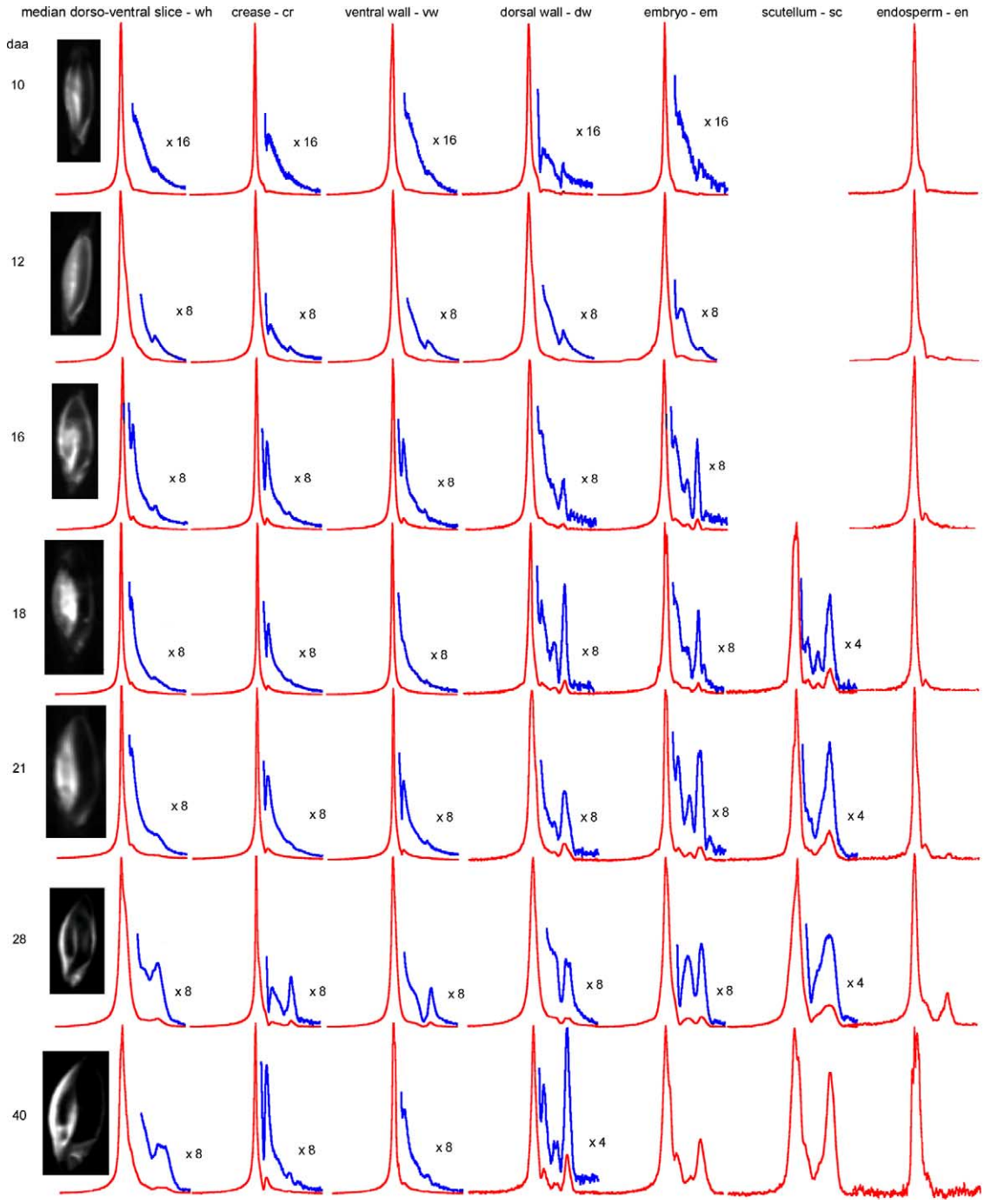

Fig. 5. NMR spectra of selected regions of lateral median 500 μm slices of barley caryopses at indicated number of days after anthesis. Spectra are individually scaled to the highest intensity peak. The images are of the total spectral range.

including the scutellum is relatively high in lipids (Fig. 4.38l). Interestingly, the endosperm shows water and soluble carbohydrate contributions in the images. By now, the ratio of lipid to water is sufficiently high for the lipid signal to show in the spectrum (Fig. 5.28w) of the whole caryopsis as well as in the embryo (Fig. 5.28em) and scutellum (Fig. 5.28sc). The signal around the outer edges of the lipid image (Fig. 4.28l) is from the aleurone layer and again this is confirmed by the spectra of these regions (Fig. 5.28vw,dw).

3.3.2. Spectra of selected areas

At 10 daa, the spectrum is mostly water in all spatial regions of the image (Fig 5.10), with a small amount of lipid visible in the embryo (Fig. 5.10em) and dorsal wall (Fig. 5.10dw). From 12 daa onwards, a small lipid peak is

visible in spectra of the whole slice (Fig. 5.*wh) and this is pronounced relative to the water peak at 28 (Fig. 5.28wh) and 40 daa (Fig. 5.40wh) as the amount of water in the caryopsis decreases. The soluble carbohydrate peak is the main feature (apart from water) of spectra of the crease region (Fig. 5.*cr) which tallies with the presence of the vascular bundle and unloading region for nutrients bound for the endosperm (Cook and Oparka, 1983). The dorsal wall region which includes the aleurone layer, contains increasing amounts of lipid relative to water with maturity (Fig. 5.*dw), as do the embryo (Fig. 5.*em) and scutellum (Fig. 5.*sc). By 40 daa, the lipid and water signals from the scutellum are comparable in intensity. Small, but increasing amounts of lipid relative to water are seen in the spectra of the endosperm (Fig. 5.*en) with a maximum at 28 daa (Fig. 5.28en). The soluble carbohydrate peak in the endosperm (Fig. 5.*en) is fairly constant relative to that for water. At 40 daa, the endosperm has largely dried out and there is very little signal as evidenced by the low signal to noise in the spectrum (Fig. 5.40en).

4. Conclusions

Taken together, the three sets of images (3D, T_2 and chemical shift) obtained at each development stage, depict the changes occurring. The principal and significant advantages of the NMR images over those obtained by light or electron microscopy are that they provide 3D images of entire living grains. No sectioning or staining for specific tissue types is involved but the spatial distribution of different chemical classes of compound can be detected in the intact, living grain. In particular, the mapping of water is not only important for an understanding of grain development, but is not accessible by conventional microscopy. The downside is that NMR images cannot compete with microscopy in terms of resolution at the cellular and sub-cellular level.

It is clear that there is the potential for water exchange between the crease and the endosperm, analogous to that described for rice (Horigane et al., 2001) which lacks the invaginated crease of barley but there is no evidence for any water supply to the embryo corresponding to the ‘central line’ described by these authors. Additionally, Horigane et al. (2001) noted the absence of a signal from the scutellum of rice whereas this is a prominent feature of the barley images from 8 daa, and in the latter stages, indicates the presence of lipid and water in similar quantities. The spatial distribution of lipid during grain development has not previously been investigated in such detail. The results obtained here demonstrate the highest lipid concentration in the embryonic axis (Price and Parson, 1979) and the scutellum (Evers and Millar, 2002) with highest levels in the scutellum. The temporal changes in lipid content broadly parallel those found by Falk et al. (2004) where the timescales of the experiments overlap. Spatial distribution of lipid at earlier stages of grain development can be inferred from the presence of lipid transfer proteins detected by tissue printing (Molina and Garciaolmedo, 1993) which are seen around the outer edge of the endosperm at around 4–8 daa (estimated from shape of images—no age given). At this early stage, almost before aleurone formation (Olsen, 2001), lipid was not apparent in the NMR images, although the image in Fig. 1.6i indicates the presence of the aleurone layer. The discrepancy may, at least in part, be due to the use of different measures of grain age: days after pollination by Olsen, and days after anther expulsion in this work. An understanding of grain development is an important facet of the underlying biology on which improvement of varieties for specific purposes is based. The NMR images reported here allow 3D examination of water and lipid distribution throughout the grain as it develops and make a further contribution to the body of fundamental knowledge on which good applied science is based.

Acknowledgements

Drs Karl Oparka, Stuart Swanston, Robbie Waugh and Brian Williamson of SCRI are gratefully acknowledged for helpful discussions. The Scottish Crop Research Institute (SCRI) is supported by the Scottish Executive Environment and Rural Affairs Department (SEERAD). Mylnefield Research Services, the commercial arm of SCRI, purchased the NMR imager.

Supplementary data

Supplementary data associated with this article can be found, in the online version, at http://www.scri.sari.ac.uk/bardev/index.htm

References

Allen, P.S., Thorne, E.T., Gardner, J.S., White, D.B., 2000. Is the barley endosperm a water reservoir for the embryo when germinating seeds are dried? International Journal of Plant Sciences 161, 195–201.

Bosnes, M., Weideman, F., Olsen, O.A., 1992. Endosperm differentiation in barley wild-type and sex mutants. Plant Journal 2, 661–674.

Briggs, D.E., 1978. Barley. Chapman and Hall, London.

Callaghan, P.T., 1993. Principles of Nuclear Magnetic Resonance Microscopy. Oxford University Press, Oxford.

Chudek, J.A., Hunter, G., 1997. Magnetic resonance imaging of plants. Progress in Nuclear Magnetic Resonance Spectroscopy 31, 43–62.

Cochrane, M.P., Duffus, C.M., 1980. The nucellar projection and modified aleurone in the crease region of developing caryopses of barley (*Hordeum vulgare* L. var. distichum). Protoplasma 103, 361–375.

Cook, H., Oparka, K.J., 1983. Movement of fluorescein into isolated caryopses of wheat and barley. Plant Cell and Environment 6, 239–242.

Donker, H.C.W., VanAs, H., Edzes, H.T., Jans, A.W.H., 1996. NMR imaging of white button mushroom (*Agaricus bisporis*) at various magnetic fields. Magnetic Resonance Imaging 14, 1205–1215.

Donker, H.C.W., VanAs, H., Snijder, H.J., Edzes, H.T., 1997. Quantitative H-1-NMR imaging of water in white button mushrooms (*Agaricus bisporus*). Magnetic Resonance Imaging 15, 113–121.

Evers, T., Millar, S., 2002. Cereal grain structure and development: Some implications for quality. Journal of Cereal Science 36, 261–284.

Falk, J., Krahnstover, A., van der Kooij, T.A.W., Schlensog, M., Krupinska, K., 2004. Tocopherol and tocotrienol accumulation during development of caryopses from barley (*Hordeum vulgare* L.). Phytochemistry 65, 2977–2985.

Fahn, A., 1967. Plant Anatomy. Pergamon Press, Oxford.

FAOSTAT, 2004. http://faostat.fao.org/faostat/default.jsp.

Glidewell, S.M., Williamson, B., Goodman, B.A., Chudek, J.A., Hunter, G., 1997. An NMR microscopic study of grape (*Vitis vinifera* L). Protoplasma 198, 27–35.

Glidewell, S.M., Williamson, B., Duncan, G.H., Chudek, J.A., Hunter, G., 1999. The development of blackcurrant fruit from flower to maturity: a comparative study by 3D nuclear magnetic resonance (NMR) micro-imaging and conventional histology. New Phytologist 141, 85–98.

Gruwel, M.L.H., Yin, X.S., Edney, M.J., Schroeder, S.W., MacGregor, A.W., Abrams, S., 2002. Barley viability during storage: Use of magnetic resonance as a potential tool to study viability loss. Journal of Agricultural and Food Chemistry 50, 667–676.

Himmelsbach, D., Gamble, G.R., 1996. Proton NMR imaging of hydration of wheat and rice grains. Journal of Magnetic Resonance Analysis 2L, 163–164.

Horigane, A.K., Toyoshima, H., Hemmi, H., Engelaar, W.M.H.G., Okubo, A., Nagata, T., 1999. Internal hollows in cooked rice grains (*Oryza sativa* cv. Koshihikari) observed by NMR micro imaging. Journal of Food Science 64, 1–5.

Horigane, A.K., Engelaar, W.M.H.G., Toyoshima, H., Ono, H., Sakai, M., Okubo, A., Nagata, T., 2000. Differences in hollow volumes in cooked rice grains with various amylose contents as determined by NMR micro imaging. Journal of Food Science 65, 408–412.

Horigane, A.K., Engelaar, W.M.H.G., Maruyama, S., Yoshida, M., Okubo, A., Nagata, T., 2001. Visualisation of moisture distribution during development of rice caryopses (*Oryza sativa* L.) by nuclear magnetic resonance imaging. Journal of Cereal Science 33, 105–114.

Ishida, N., Koizumi, M., Kano, H., 1996. Location of sugars in barley seeds during germination by NMR microscopy. Plant Cell and Environment 19, 1415–1422.

Kano, H., Ishida, N., Kobayashi, T., Koizumi, M., 1990. H-1-NMR Imaging analysis of changes of free-water distribution in barley and soybean seeds during maturation. Japanese Journal of Crop Science 59, 503–509.

McEntyre, E., Ruan, R., Fulcher, R.G., 1998. Comparison of water absorption patterns in two barley cultivars, using magnetic resonance imaging. Cereal Chemistry 75, 792–795.

Meiboom, S., Gill, D., 1958. Modified spin-echo method for measuring nuclear relaxation times. Review of Scientific Instruments 29, 688–691.

Molina, A., Garciaolmedo, F., 1993. Developmental and pathogen-induced expression of 3 barley genes encoding lipid transfer proteins. Plant Journal 4, 983–991.

Molina-Cano, J.-L., Sopena, A., Polo, J.P., Bergareche, C., Moralejo, M.A., Swanston, J.S., Glidewell, S.M., 2002. Relationships between barley hordeins and malting quality in a mutant of cv. *Triumph*. II. Genetic and environmental effects on water uptake. Journal of Cereal Science 36, 39–50.

Olsen, O.A., 2001. Endosperm development: cellularization and cell fate specification. Annual Review of Plant Physiology and Plant Molecular Biology 52, 223–267.

Price, P.B., Parson, J., 1979. Distribution of lipids in embryonic axis, bran-endosperm, and hull fractions of hulless barley and hulless oat grain. Journal of Agricultural and Food Chemistry 27, 813–815.

Ruan, R., Litchfield, J.B., 1992. Determination of water distribution and mobility inside maize kernels during steeping using magnetic resonance imaging. Cereal Chemistry 69, 13–17.

Ruan, R., Litchfield, J.B., Eckhoff, S.R., 1992. Simultaneous and nondestructive measurement of transient moisture profiles and structural changes in corn kernels during steeping using microscopic nuclear magnetic resonance imaging. Cereal Chemistry 69, 600–606.

Ruan, R.R., Chen, P.L., Almaer, S., 1999. Nondestructive analysis of sweet corn maturity using NMR. Hortscience 34, 319–321.

Song, H.P., Delwiche, S.R., Line, M.J., 1998. Moisture distribution in a mature soft wheat grain by three- dimensional magnetic resonance imaging. Journal of Cereal Science 27, 191–197.

Takeuchi, S., Maeda, M., Gomi, Y., Fukuoka, M., Watanabe, H., 1997. The change of moisture distribution in a rice grain during boiling as observed by NMR imaging. Journal of Food Engineering 33, 281–297.

The Maltsters Association of Great Britain, 2004. Use of barley for malting. http://www.ukmalt.com/maltindustry/industry.html.

Wallwork, M.A.B., Jenner, C.F., Logue, S.J., Sedgley, M., 1998. Effect of high temperature during grain-filling on the structure of developing and malted barley grains. Annals of Botany 82, 587–599.

Weschke, W., Panitz, R., Sauer, N., Wang, Q., Neubohn, B., Weber, H., Wobus, U., 2000. Sucrose transport into barley seeds: Molecular characterization of two transporters and implications for seed development and starch accumulation. The Plant Journal 21, 455–467.

Xia, Y., Jelinski, L.W., 1995. Imaging low-concentration metabolites in the presence of a large background signal. Journal of Magnetic Resonance Series B 107, 1–9.